Polarimetric Scattering From Two-Layered Two-Dimensional Random Rough Surfaces With and Without Buried Objects

Magda El-Shenawee, *Senior Member, IEEE*

***Abstract*—A three-dimensional polarimetric analysis of the two-layered rough ground with and without buried objects is investigated here. A rigorous electromagnetic surface integral-equation-based model is used in this analysis. The statistical average of the polarimetric scattering matrix elements is computed based on the Monte Carlo simulations for both the vertically and horizontally polarized incident waves. The results show a significant impact on the scattered intensities due to the two-layer nature of the ground. However, these intensities show almost no difference between the ground signature with or without the object. On the other hand, the statistical average of the covariance matrix elements shows a distinct difference between these two signatures despite the small size of the buried object.**

***Index Terms*—Computational electromagnetics, multilayered rough ground, rough surface scattering.**

I. Introduction

ELECTROMAGNETIC sensing of buried objects in the presence of random rough interfaces is important for subsurface detection problems in general. An observation agreed upon by most theoreticians and experimentalists that the surface roughness constitutes a major source of clutter (i.e., noise) in the received electromagnetic signals. The two-dimensional (2-D) rough surface ground (i.e., three-dimensiaonl (3-D) scattering problem) is the more realistic problem as investigated by many researchers [1]–[8]. These publications presented scattering from rough surfaces with *no buried objects*. In addition, works on modeling electromagnetic waves scattered from single or multiple objects located above or buried beneath the 2-D random rough ground were reported in [9]–[15].

In all work cited above, the rough ground surface was assumed a single homogeneous layer. There are few works published to model scattering from two-layered rough surfaces with *no buried objects* [16], [17]. In addition, the scattering from a general 3-D dielectric target embedded in a two-layered half-space medium was investigated using the method of moments (MoM) as reported in [18]. However, all interfaces in [18] were assumed *flat* surfaces. Because of the significant impact of ground roughness on the scattered signature as discussed in [9]–[15], it is important to incorporate the ground roughness in all interfaces involved in the model. This issue is important in order to model the ground as close as possible to the real situation. The objective of this work is to analyze the fully polarimetric electromagnetic wave scattering from two-layered random rough ground with and without the presence of a 3-D penetrable buried object. The two-layer ground, will be modeled by two homogeneous layers where both interfaces are random rough surfaces. This implies that the involved three homogeneous layers are: the air, the upper ground layer with finite thickness H, and the underground layer with infinite depth as shown in Fig. 1. This complex scenario will be analyzed using the steepest descent fast multipole method (SDFMM), which has $O(N)$ computational complexity, where N is the number of surface current unknowns [19]. The SDFMM has been successfully implemented for a variety of subsurface sensing applications [11]–[15].

The geometry of the current application is shown in Fig. 1 where a dielectric object is buried between the air- and the underground rough interfaces. The depth of the underground interface should be less than one free-space wavelength to satisfy the quasiplanar structure constraint of the SDFMM [19].

The formulations of the problem were derived in previous work [13], [14] where the ground was a single-layer. For convenience, these formulations are summarized in Section II and in the Appendix. The numerical results are presented in Section III, and concluding remarks are given in Section IV.

II. Formulation

The inhomogeneous structure, analyzed here, is shown in Fig. 1, which is composed of four different homogeneous regions as follows: the air (R_1), the upper ground layer (R_2), the buried object (R_3), and the lower ground layer (R_4). These regions have relative permittivity and permeability as (ε_1 and μ_1), (ε_2 and μ_2), (ε_3 and μ_3), and (ε_4 and μ_4), respectively. The surface integral equation-based model, derived in [13] and [14], is used to calculate the unknown equivalent surface currents on all scatterers in Fig. 1. For convenience, these formulations are given in the Appendix. Upon simulating the incident waves by a carefully tapered Gaussian beam [20], the excitation on the ground surface away from the footprint center can be neglected. This leads to analyze the closed surfaces S_1 and S_3 as open interfaces [11]–[15]. In order to apply the MoM, and consequently the SDFMM, these surfaces are discretized into the Rao–Wilton–Glisson (RWG) triangular patches [21], [22]. After some algebraic manipulations, the unknown equivalent electric

Manuscript received October 25, 2002; revised April 21, 2003. This research was supported in part by the Arkansas Science and Technology Authority (ASTA) under Grant AR/ASTA/01-B-18, in part by the Northeastern University's Demining Multidisciplinary University Research Initiative (MURI) under Grant DAA 0-55-97-0013, and in part by the Northeastern University ERC-NSF under Award EEC-9986821.

The author is with the Department of Electrical Engineering, University of Arkansas, Fayetteville, AR 72701 USA (e-mail: magda@uark.edu).

Digital Object Identifier 10.1109/TGRS.2003.815675

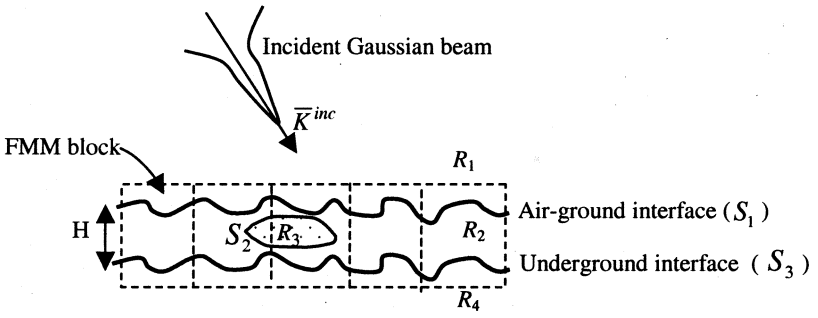

Fig. 1. Cross section of the two-layered rough ground showing the FMM finest blocks (3-D scattering problem).

and magnetic surface currents $\overline{J}_1$ and $\overline{M}_1$ (on the air–ground interface), $\overline{J}_2$ and $\overline{M}_2$ (on the buried object), and $\overline{J}_3$ and $\overline{M}_3$ (on the underground interface) are obtained by solving the linear system of equations $\overline{\overline{Z}}\overline{I} = \overline{V}$. The square impedance matrix $\overline{\overline{Z}}$ has order of $2(N_1 + N_2 + N_3)$, where the total number of current unknowns on the air–ground interface is $2N_1$, on the buried object is $2N_2$ and on the underground interface is $2N_3$. The vector $\overline{V}$ represents the tested tangential incident electric field $\overline{E}^{\,\mathrm{inc}}$ and the normalized magnetic field $\eta_1\overline{H}^{\,\mathrm{inc}}$ on the air–ground interface. The matrix $\overline{\overline{Z}}$ is given by

$$\overline{\overline{Z}} = \begin{bmatrix} \overline{Z}_{11} & \overline{Z}_{12} & \overline{Z}_{13} \\ \overline{Z}_{21} & \overline{Z}_{22} & \overline{Z}_{23} \\ \overline{Z}_{31} & \overline{Z}_{32} & \overline{Z}_{33} \end{bmatrix} \tag{1}$$

in which the submatrices $\overline{Z}_{11}$, $\overline{Z}_{22}$, and $\overline{Z}_{33}$ represent the self-interactions on the air–ground interface, the buried object, and the underground interface, respectively. On the other hand, the submatrices $\overline{Z}_{12}$ (and $\overline{Z}_{21}$) and $\overline{Z}_{13}$ (and $\overline{Z}_{31}$) represent the interactions between the air–ground interface with the buried object and with the underground interface, respectively. The submatrices $\overline{Z}_{32}$ (and $\overline{Z}_{23}$) represent the interactions between the underground interface and the buried object. The SDFMM is implemented to dramatically accelerate the solution of the unknown surface current coefficients $\overline{I}$, and consequently to obtain the vector surface currents $\overline{J}$ and $\overline{M}$ on all surfaces (as given in the Appendix).

If the MoM is used to solve the linear system of equations $\overline{\overline{Z}}\overline{I} = \overline{V}$, it requires computing and storing all elements of the matrix $\overline{\overline{Z}}$ and then multiplying them by the vector $\overline{I}$. This is considered a very expensive computational process for the two-layered configuration where the total matrix $\overline{\overline{Z}}$ contains two large submatrices $\overline{Z}_{11}$ and $\overline{Z}_{33}$ associated with the two rough interfaces shown in Fig. 1. However, upon using the SDFMM [11] and [19], the above system of equations can be rewritten as $\overline{\overline{Z}}'\overline{I} + \overline{\overline{Z}}''\overline{I} = \overline{V}$, where the matrix $\overline{\overline{Z}}'$ becomes sparse. This implies that only the nonzero elements need to be calculated and stored using the conventional MoM and then multiplying $\overline{\overline{Z}}'$ by the vector $\overline{I}$. This process is considered the near-field interactions. On the other hand, the matrix–vector multiply $\overline{\overline{Z}}''\overline{I}$ is computed in one step without calculating or storing any elements of the matrix $\overline{\overline{Z}}''$, which is achieved using the FMM hybridized with the SDP integration rule [19]. This process is considered the far-field interactions.

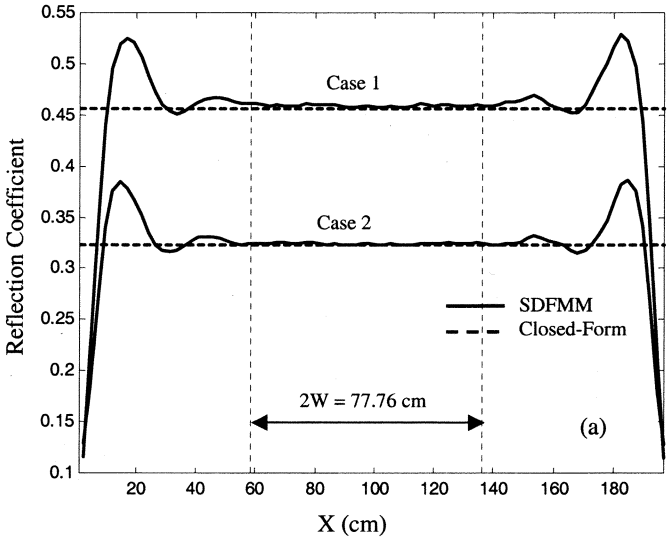

Fig. 2. Reflection coefficient for two-layer ground with no objects and dimensions are 194.4 cm × 194.4 cm. In Case 1, $\varepsilon_{r2} = 2.5 - j0.18$ and $\varepsilon_{r4} = 9.8 - j1.2$. In Case 2, $\varepsilon_{r2} = 2.5 - j0.18$ and $\varepsilon_{r4} = 4.3 - j0.2$. Normal incidence is used.

The expressions of all submatrices elements are explained in detail in [13] and [14]. It is important to emphasize that the 3-D geometry investigated in [13] and [14] is composed of the air–ground rough interface and two dielectric objects buried in the ground, where the size of both objects was small compared with the free-space wavelength. On the other hand, in the current configuration, all submatrices are computed using the fast multipole technique except $\overline{Z}_{22}$, which is computed using the MoM. The later submatrix represents the impedance matrix of the buried object, which has a small size compared with the upper or the lower ground interfaces.

The configuration of Fig. 1 has potential for several applications, e.g., the antipersonnel and antitank mine detection where the target could be buried in two-layered ground. This situation could easily occur in Bosnian or Cambodian land-mine fields where snow or vegetation layers could be present above the soil ground. In some situations, the ground could be inhomogeneous with dielectric constant varying at each point. This is not the problem to be investigated here, since the surface integral equations-based model is not suitable for such a situation. In the current work, the ground is modeled by two homogeneous rough layers.

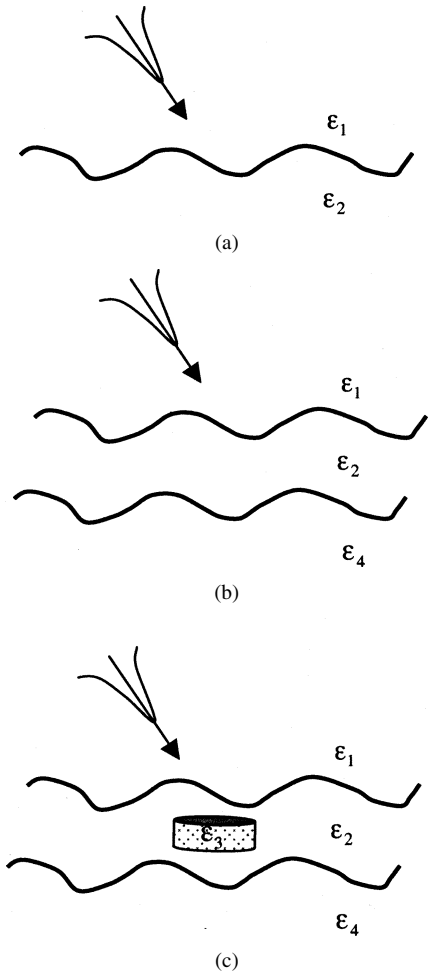

Fig. 3. Geometry cross section for (a) single-layer rough ground, (b) two-layer rough ground, and (c) two-layer rough ground with buried object.

III. Numerical Results

The two rough interfaces depicted in Fig. 1 are characterized with Gaussian statistics for the height and the autocorrelation function [23]; however, each interface has different ground roughness parameters. The roughness of the upper and lower interfaces were randomized by considering them as flat surfaces discretized into the RWG triangular patches [21], [22]. Then the heights of the surface nodes are assumed random variables with Gaussian probability density function. Also, the correlation between any two points on each surface is assumed Gaussian, as described in [23]. The Monte Carlo simulations are needed to draw conclusions based on the average of several realizations, while the results of individual realizations are used for a parametric study. The normalized RCS is defined by $4\pi r^2 \left|\overline{E}^S\right|^2 / \left(2\eta_0 P^i A_z\right)$, where A_z is the footprint area, P^i is the incident power, η_0 is the intrinsic impedance, and $\left|\overline{E}^S\right|$ is the magnitude of the scattered electric field. All the RCS results in this work are presented as RCS/λ_0^2, where λ_0 is the free-space wavelength in meters. The transpose-free quasi-minimal iterative solver (TFQMR) is used with a tolerance of 10^{-3} [24].

The dimensions of the two-layered ground are assumed $6.48\lambda_0 \times 6.48\lambda_0$ and $8\lambda_0 \times 8\lambda_0$, respectively. When both interfaces are of dimensions $6.48\lambda_0 \times 6.48\lambda_0$, the number of electric and magnetic surface current unknowns on each interface is 39 042 (i.e., the total number of unknowns on the ground is 78 084). As known, for dielectric scatterers, the numerical accuracy of the solution enhances with decreasing the discretization length (e.g., $0.1\lambda_g$, where $\lambda_g < \lambda_0$ is the wavelength in the medium). In all results, the discretization length is assumed to be $0.08\lambda_0$, since moderate values for the ground dielectric constants are used in this section. In addition, the correlation length assumed for the rough interfaces, $0.4\lambda_0$–$0.5\lambda_0$, are equal to several discretization lengths, which is necessary to capture the ground roughness.

For the $6.48\lambda_0 \times 6.48\lambda_0$ ground dimensions, the half beam width of the Gaussian beam is assumed ($6.48\lambda_0/5 = 1.296\lambda_0$), which guarantees good attenuation of the fields at the ground edges (-28 dB) [4], [5], [11]–[15]. This indicates that the incident beam illuminates the ground with plane waves over a spot of diameter equal to $2.59\lambda_0$ (i.e., the footprint) centered at $x = y = 3.24\lambda_0$. It is important to emphasize that the incident beam footprint is carefully chosen to be much larger than the width of the buried object. For ground with dimensions $8\lambda_0 \times 8\lambda_0$, the total number of unknowns becomes 119 200. It is computationally more efficient to model the ground with dimensions $6.48\lambda_0 \times 6.48\lambda_0$, in order to conduct Monte Carlo simulations based on a 100 2-D rough surface realizations for both the vertical and horizontal polarizations and for single- and two-layered rough ground. However, examples for individual rough surface realizations for the $8\lambda_0 \times 8\lambda_0$ ground were computed but not shown here. The dimensions of the buried object will be given in each example presented here.

A. Validation

To validate the SDFMM computer code for the configuration in Fig. 1, the numerical solution of a modeled two-layer flat ground with *no buried objects* is compared with that obtained using the closed form for the semi-infinite two-layered flat ground. In one case, the relative dielectric constants of the upper and lower ground layers are $\varepsilon_{r2} = 2.5 - j0.18$ (Bosnian soil with 3.8% moisture) and $\varepsilon_{r4} = 9.8 - j1.2$ (Bosnian soil with 25% moisture) at 1 GHz [25], respectively. In the second case, the relative dielectric constant of the upper layer is the same as before, while the lower ground layer is assumed $\varepsilon_{r4} = 4.3 - j0.2$. A 10-cm thickness ($H$ in Fig. 1) is assumed for the upper ground layer. The modeled ground is excited with plane waves tapered toward the edges to eliminate edges excitations (e.g., by using a Gaussian beam as discussed earlier) [20], while the semi-infinite ground is excited with plane waves every where. The comparison for the ground with dimensions 194.4 cm × 194.4 cm (i.e., $6.48\lambda_0 \times 6.48\lambda_0$ at 1 GHz) is shown in Fig. 2 for both cases. The comparison is based on the reflectivity Γ (or the power reflection coefficient), which is defined as the normal components of the time-average Poynting's vector ($\overline{S}_a = \mathrm{Re}\left(\overline{\mathrm{E}} \times \overline{\mathrm{H}}^*\right)/2$), given by $\Gamma = \left(\hat{z} \cdot \overline{S}_{ar}\right) / \left(-\hat{z} \cdot \overline{S}_{ai}\right)$ [26]. The subscripts r and i represent the reflected and incident waves, respectively, and $\hat{z}$ is the unit vector normal to the flat interface (x and y directions). The SDFMM is used to calculate the unknown surface currents on the two flat interfaces; then, the scattered electric and magnetic fields are calculated just above the air–ground interface using the near-field formulations given in [27, ch. 6]. Those formulations are numerically invalid if the

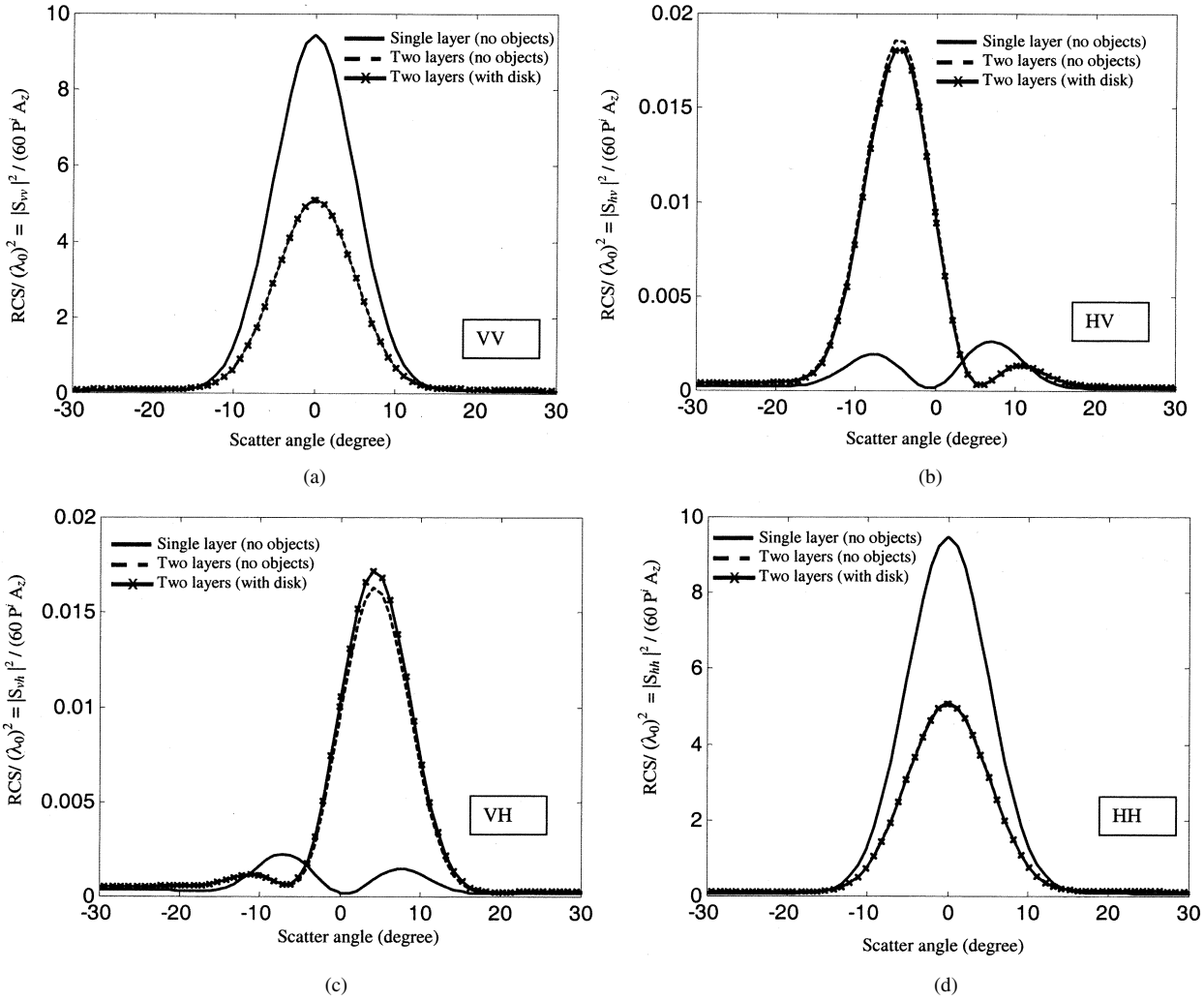

Fig. 4. Statistical average of the normalized RCS for (a) VV, (b) HV, (c) VH, and (d) HH. The average is based on Monte Carlo simulations of 100 rough surface realizations. Normal incidence.

fields are calculated exactly on the ground, since the distance between the source and observation points becomes zero in this case. Several numerical experiments were conducted (not presented here) showing that the minimum distance between the source and observation points should not be less than be $0.1\lambda_0$ in order to use the near-field formulations of [27]. The reflection coefficient, which is the square root of the reflectivity Γ, is plotted versus the x direction of the ground at $y = 3.24\lambda_0$, as shown in Fig. 2. The comparison shows that the numerical solution agrees with the closed form within the footprint area of 77.76 cm $\times$ 77.76 cm (i.e., the area $2.592 \times 2.592\lambda_0$ at 1 GHz), which represents the spot size of incident plane waves. Notice that there are slight oscillations in the SDFMM numerical results, which are due to the standing waves caused by small excitations of the truncated ground edges as discussed in [28]. It is important to mention that the SDFMM was validated with other numerical techniques for scattering from single-layer rough ground surface with and without buried objects as reported in [11].

The computer memory and total CPU time required for $6.48\lambda_0 \times 6.48\lambda_0$ two-layer flat ground solution, shown in Fig. 2, are 1.8 GB and 2.7 h, respectively. The solution for the $8\lambda_0 \times 8\lambda_0$ two-layer ground (not presented here) required 3 GB and 4.6 h, respectively. These results are obtained using the COMPAQ ALPHA server 667-MHz machine. The SDFMM finest block size is assumed $0.32\lambda_0$, with two blocks separating the near- to far-field limits [19].

B. Polarimetric Scattering Based on Monte Carlo Simulations (Statistical Averaging)

The scattering matrix elements $S_{\rm vv}$, $S_{\rm hv}$, $S_{\rm vh}$, and $S_{\rm hh}$ for the configurations in Fig. 3(a)–(c) are computed and plotted for the bistatic case. The results presented in this subsection are the average of 100 Monte Carlo simulations. This implies that the scattering from the same 100 rough surface realizations is computed six times. These runs include computing the scattering from the single-layer ground with *no buried objects* and the scattering from the two-layer ground *with and without buried objects*, for both the horizontal and vertical incident polarizations. The normalized RCS for $S_{\rm vv}$, $S_{\rm hv}$, $S_{\rm vh}$, and $S_{\rm hh}$ are plotted in Fig. 4(a)–(d), respectively. A normal incident angle is used in all results in this section. For the single-layer rough ground shown in Fig. 3(a), the dielectric constant is assumed $\varepsilon_{r2} = 2.5 - j0.18$, while the ground roughness parameters are assumed as $\sigma =$

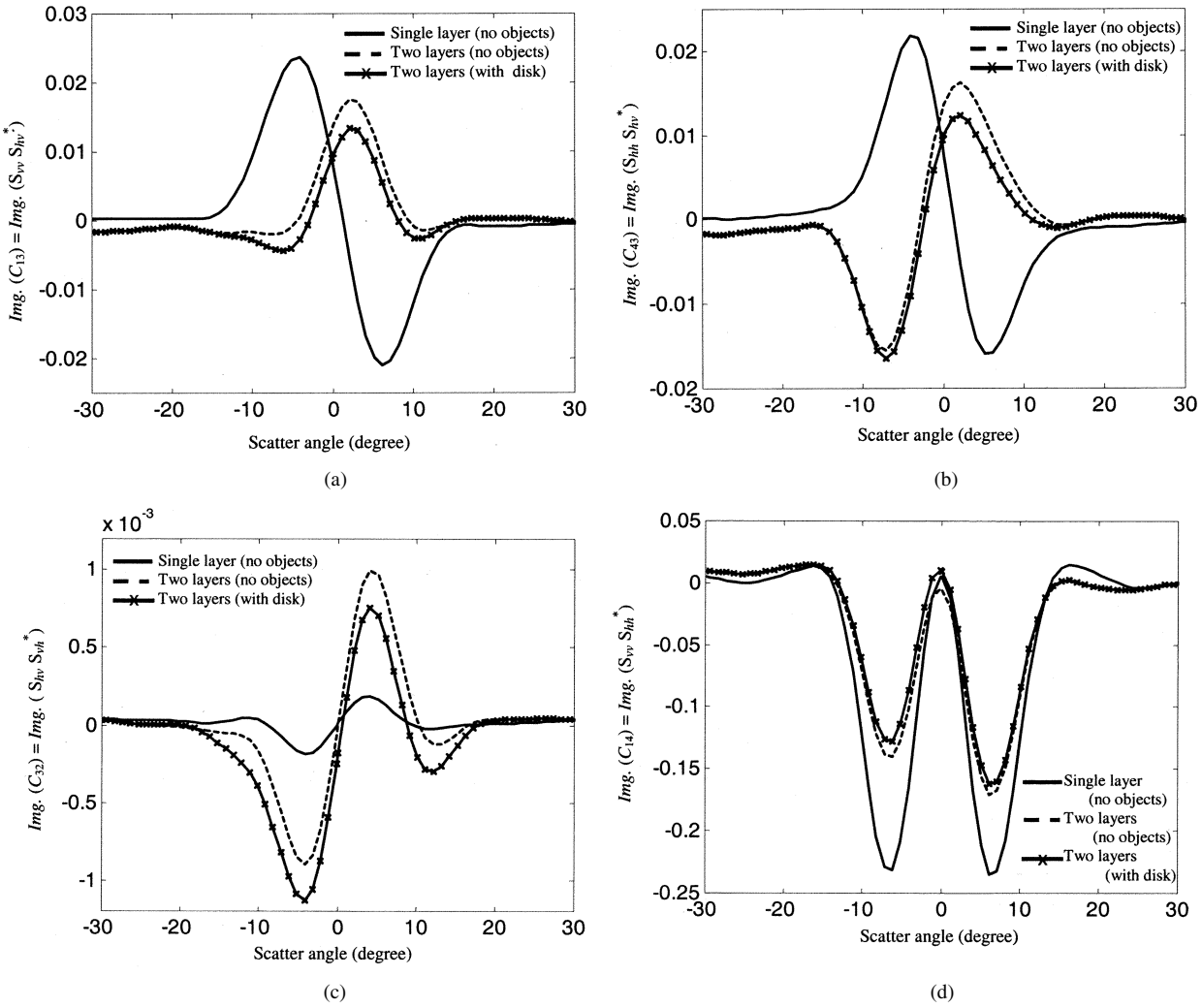

Fig. 5. Statistical average of the imaginary part of the Covariance matrix elements as (a) C_{13}, (b) C_{43}, (c) C_{32}, and (d) C_{14}, for the same data of Fig. 4.

$0.05\lambda_0$ (rms height) and $l_c = 0.4\lambda_0$ (correlation length). For the two-layer rough ground shown in Fig. 3(b), the dielectric constants are $\varepsilon_{r2} = 2.5 - j0.18$ and $\varepsilon_{r4} = 4.3 - j0.6$ for the upper and lower layers, respectively. The thickness of the upper layer is $H = 0.5\lambda_0$ and the ground roughness parameters are $\sigma_1 = 0.05\lambda_0$, $l_{c1} = 0.4\lambda_0$ and $\sigma_2 = 0.04\lambda_0$, $l_{c2} = 0.5\lambda_0$ for the upper and lower interfaces, respectively. For the two-layer rough ground with a buried disk shown in Fig. 3(c), the parameters of the ground are the same as in Fig. 3(b). The buried disk has a radius of $a = 0.166\lambda_0$, a height of $h = 0.14\lambda_0$, and is buried at $z = -0.2\lambda_0$ measured from its top surface. The dielectric constant of the disk is similar to the TNT plastic mine given by $\varepsilon_{r3} = 2.9 - j0.0029$ [25]. The results of Fig. 4(a)–(d) show a significant difference between the RCS of the single-layer ground compared with that of the two-layer ground for all co- and cross-polarizations. In particular, the copolarized RCS of the single-layer rough ground is larger than that of the two-layer rough ground with or without the buried disk. On the other hand, the cross-polarized RCS of the two-layer ground is larger than that of the single-layer ground. This implies that the multilayer nature of the ground increases the depolarization of electromagnetic waves. As known, the RCS for the H- and V-cross-polarizations in Fig. 4(b) and (c) should be exactly equal in the backscatter direction, i.e., at normal incidence in this case. However, these figures show a slight difference between the VH and the HV results at $\vartheta^i = 0^\circ$. This numerical error could be due to the insufficient size of the Monte Carlo sample, which may need to be increased, or it could be due to inherited computational accuracy. Interestingly, it is observed that the VH and HV results in Fig. 4(b) and (c) are asymmetric around the scatter angle 0, only when considering the two-layer ground. New numerical results (not presented here) are obtained for the VV and HV at several heights $H = 0.3\lambda_0$–$0.7\lambda_0$, with steps of 0.1 λ_0 or less for the same individual rough surface realization (no averaging). These runs show that the HV results are almost symmetric at small heights $H = 0.3\lambda_0$–$0.4\lambda_0$; then, they gradually become more asymmetric at heights $H = 0.42\lambda_0$–$0.55\lambda_0$, and finally they gradually become symmetric again at $H = 0.6\lambda_0$–$0.7\lambda_0$. The results show that changing the height H affects both the magnitude and the peak location of the HV; however, it only affects the magnitude of the VV, which is always symmetric around zero. This could be because of the random multiple interactions between the upper and lower interfaces that mostly affects the symmetry of the cross-polarized scattered fields.

It is clear that the increase in the wave depolarization when the ground has two layers is not due to the presence of the buried

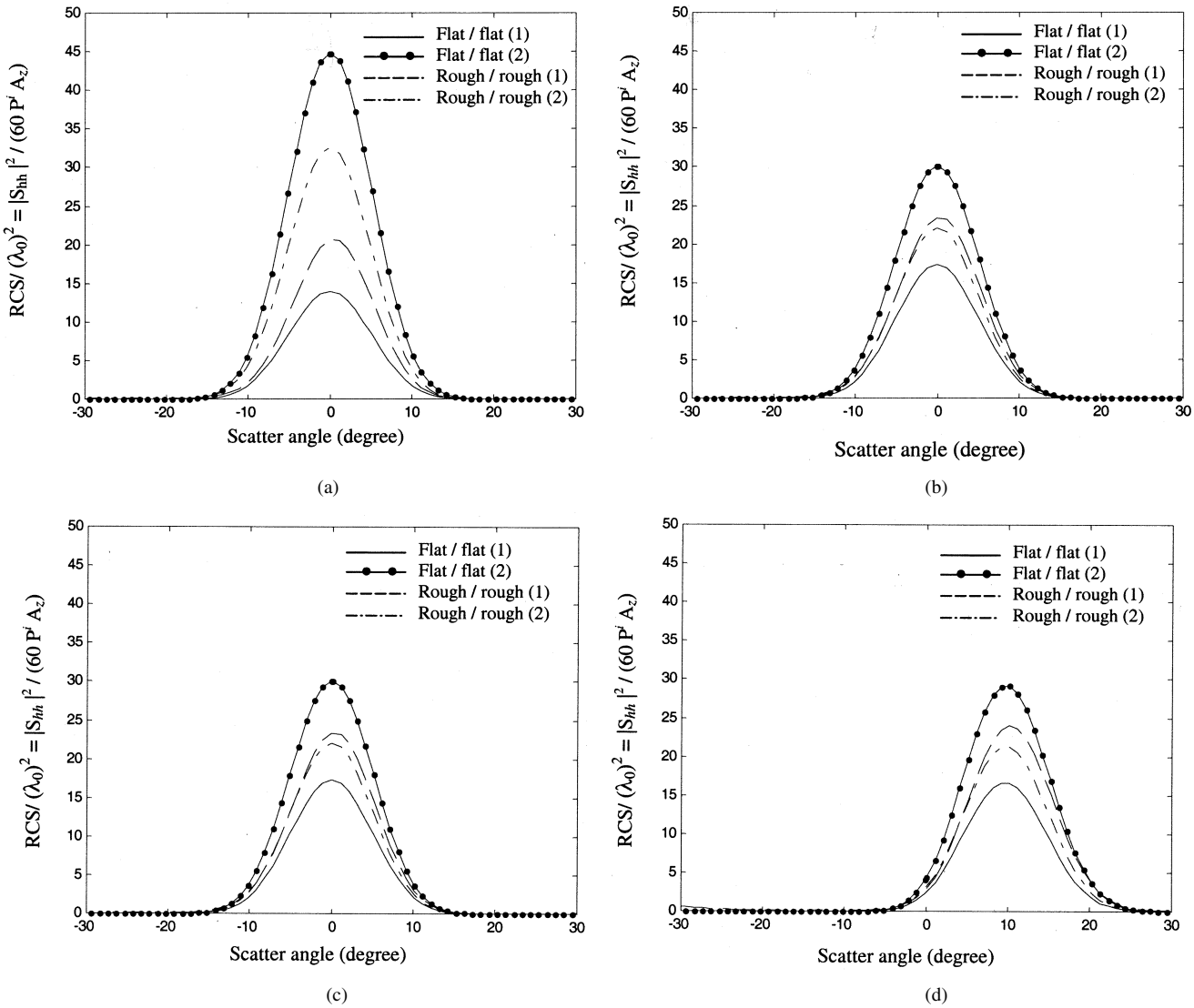

Fig. 6. Normalized RCS for (a) lossless two-layered ground with no buried objects for Case 1 ($\varepsilon_{r2} = 6.5$, $\varepsilon_{r4} = 2.5$), and Case 2 ($\varepsilon_{r2} = 2.5$, $\varepsilon_{r4} = 6.5$), (b) lossy two-layered ground with buried spheroid of $\varepsilon_{r3} = 2.9 - j0.0029$, Case 1 ($\varepsilon_{r2} = 6.5 - j0.1$, $\varepsilon_{r4} = 2.5 - j0.18$), and Case 2 ($\varepsilon_{r2} = 2.5 - j0.18$, $\varepsilon_{r4} = 6.5 - j0.1$), (c) lossy multilayered ground with no buried objects for same data of Fig. 6(b) without the object, and (d) same data of (b) but at $\vartheta^i = 10°$. H-polarization, results (a)–(c) are at normal incidence.

object, since the depolarization increased even when no objects were buried in the ground as shown in Fig. 4(b) and (c). This observation could be due to the wave multiple interactions between the upper and lower rough interfaces.

All results in Fig. 4(a)–(d) show that the buried disk signature is almost invisible agreeing with the previous work in [11]–[15], which motivated the search for another distinguishable characteristic using the complex covariance matrix $\overline{C}$ given by [29]

$$\overline{C} = \begin{bmatrix} S_{\rm vv}S_{\rm vv}^* & S_{\rm vv}S_{\rm vh}^* & S_{\rm vv}S_{\rm hv}^* & S_{\rm vv}S_{\rm hh}^* \\ S_{\rm vh}S_{\rm vv}^* & S_{\rm vh}S_{\rm vh}^* & S_{\rm vh}S_{\rm hv}^* & S_{\rm vh}S_{\rm hh}^* \\ S_{\rm hv}S_{\rm vv}^* & S_{\rm hv}S_{\rm vh}^* & S_{\rm hv}S_{\rm hv}^* & S_{\rm hv}S_{\rm hh}^* \\ S_{\rm hh}S_{\rm vv}^* & S_{\rm hh}S_{\rm vh}^* & S_{\rm hh}S_{\rm hv}^* & S_{\rm hh}S_{\rm hh}^* \end{bmatrix}. \quad (2)$$

Notice that the diagonal elements of the Covariance matrix $\overline{C}$ in (2) are the amplitude squared of the scattering matrix elements. In Fig. 5(a)–(d), the statistical average of the imaginary part of the elements $C_{13} = S_{\rm vv}S_{\rm hv}^*$, $C_{43} = S_{\rm hh}S_{\rm hv}^*$, $C_{32} = S_{\rm hv}S_{\rm vh}^*$ and $C_{14} = S_{\rm vv}S_{\rm hh}^*$ are plotted for all geometries of Fig. 3(a)–(c). The statistical average is conducted based on 100 rough surface realization results. The results of Fig. 5 show that the buried disk's signature is clearly distinguishable, which is not the case in Fig. 4. However, the statistical average of the real parts of the same covariance matrix elements did not show a distinguishable signature for the buried disk (not presented). This observation could be interpreted upon representing the Stokes vector elements, and consequently the covariance matrix elements, as functions of the ellipticity angle χ of the polarization ellipse (a discussion in [29, ch. 1]). In this representation, the imaginary part becomes a function of $\sin(2\chi)$, while the real part becomes a function of $\cos(2\chi)$. Notice that the sign of χ determines the handedness of the polarization state to be left-handed when $\chi > 0$, and right-handed when $\chi < 0$ [29]. In other words, the imaginary part contains more information about the polarization state (i.e., the sign of χ) than the real part as shown in Fig. 5. These results agree with the conclusions reported by Narayanan *et*

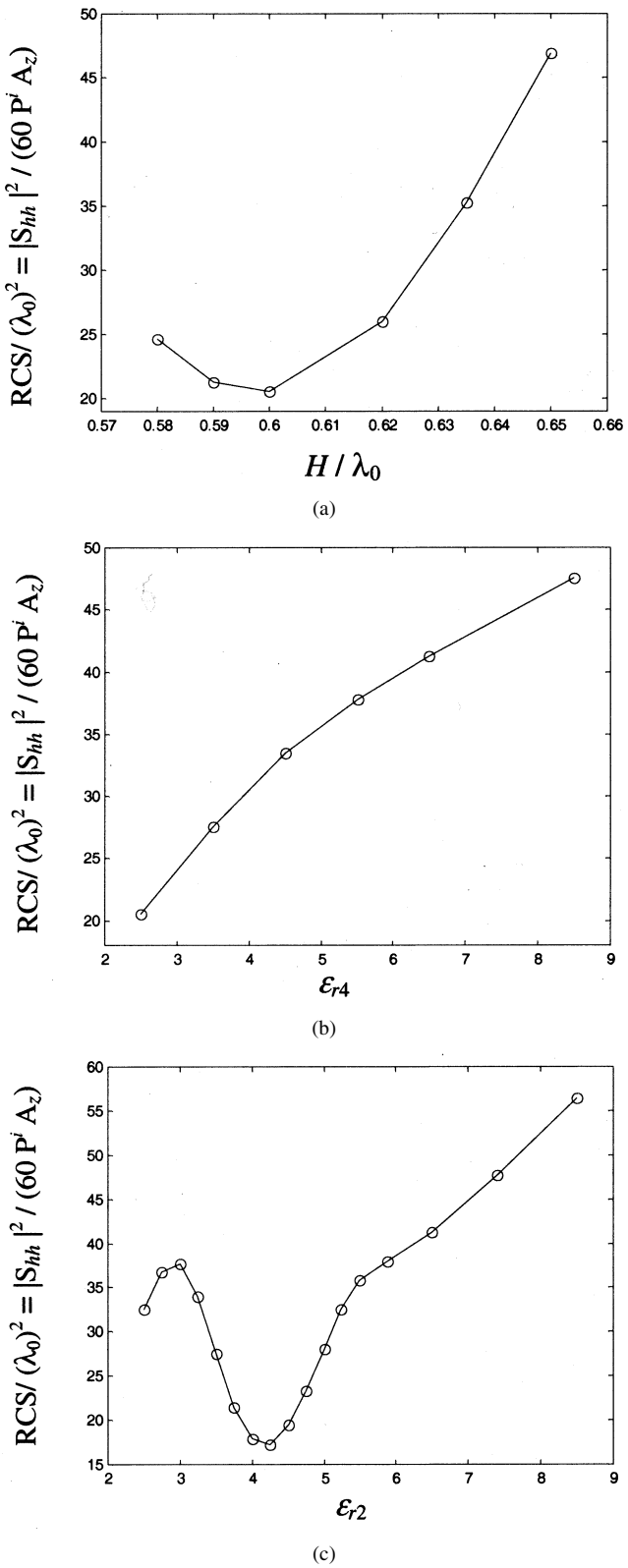

Fig. 7. Normalized RCS at backscatter versus (a) the height H where $\varepsilon_{r2} = 6.5$ and $\varepsilon_{r4} = 2.5$, (b) ε_{r4}, where $\varepsilon_{r2} = 6.5$ and $H = 0.6\lambda_0$, and (c) ε_{r2}, where $\varepsilon_{r4} = 6.5$ and $H = 0.6\lambda_0$. The spheroid is buried at $z = -0.3\lambda_0$, with $\varepsilon_{r3} = 2.9$. H-polarization at normal incidence.

al. [30], where their results presented experimental images for buried objects collected using the polarimetric coherent random noise radar operated at the University of Nebraska. It is important to mention that plotting the imaginary parts of the elements $S_{\rm vv}$, $S_{\rm hv}$, $S_{\rm vh}$, and $S_{\rm hh}$ (not presented) do not show a distinguishable signature for the target [15].

The total number of Monte Carlo simulations conducted in this subsection is 400 for the two-layer case and 200 for the single-layer case. The CPU time needed to obtain the results from one rough surface realization (i.e., one simulation) is 54 min for the single-layer ground, 180 min for the two-layered ground with no buried objects, and 340 min for the two-layer ground with buried disk. Notice the dramatic increase in the CPU needed for the two-layer rough ground with a buried object compared with the flat ground with no buried objects discussed in Section III-A. The total CPU time needed to obtain the results presented in this subsection is $2 \times (100 \times 54 + 100 \times 180 + 100 \times 340) = 114\,800$ min (i.e., 78 days), where the multiplication by two is to account for the vertically and horizontally polarized incident waves.

Even though the scattering mechanism from the buried object is deterministic, however, the object's signature is embedded in the random signature of the ground, which necessitates conducting the Monte Carlo simulations.

C. Parametric Investigations Based on Individual Rough Surface Realization (No Averaging)

An investigation based on the thickness H, the roughness parameters σ and l_c, the relative dielectric constants ε_{r2} and ε_{r4}, and the incident angle ϑ^i is conducted in this subsection. However, all results are based on individual rough surface realizations (i.e., no averaging). In the first example, both the air- and underground interfaces are random rough surfaces with roughness parameters as $\sigma_1 = 0.04\lambda_0$, $l_{c1} = 0.5\lambda_0$ and $\sigma_2 = 0.03\lambda_0$, $l_{c2} = 0.4\lambda_0$, respectively. To investigate the roughness effect, numerical results are also obtained when the air- and underground interfaces are flat surfaces (i.e., flat/flat) and when the air–ground interface is flat but the underground interface is rough (i.e., flat/rough) and visa versa. The mean of the underground interface in this example is located at $z = -0.6\lambda_0$, i.e., $H = 0.6\lambda_0$. In Fig. 6(a), the two regions are assumed lossless with *no buried objects* and the relative dielectric constants are $\varepsilon_{r2} = 6.5$ and $\varepsilon_{r4} = 2.5$ in case 1, and $\varepsilon_{r2} = 2.5$ and $\varepsilon_{r4} = 6.5$ in case 2. In Fig. 6(b), the two regions are assumed lossy with $\varepsilon_{r2} = 6.5 - j0.1$ and $\varepsilon_{r4} = 2.5 - j0.18$ in Case 1 and $\varepsilon_{r2} = 2.5 - j0.18$, and $\varepsilon_{r4} = 6.5 - j0.1$ in Case 2, where a spheroid with dimensions $a = c = 0.3\lambda_0$, $b = 0.15\lambda_0$, is buried at $z = -0.3\lambda_0$ measured from its center. In this case, the dielectric constant of the spheroid is $\varepsilon_{r3} = 2.9 - j0.0029$ [11]–[15]. In Fig. 6(c), the previous data of Fig. 6(b) are used but with *no spheroid* buried in the ground. The incident angle is $\vartheta^i = 0^\circ$ in Fig. 6(a)–(c) and is 10° in Fig. 6(d). The same data of Fig. 6(b) was used in Fig. 6(d) except for the incident angle. The results of Fig. 6(a) show, as expected, larger magnitudes in the lossless case than those in the lossy cases in Fig. 6(b)–(d). Moreover, in Fig. 6(a)–(c), the magnitudes for the flat/flat in Case 2 are larger than those for the flat/flat in Case 1. Similar observation is shown for the lossless case when both interfaces are rough surfaces; however, for the lossy cases in Fig. 6(b) and (c), the magnitudes for Case 1 are slightly larger than those for Case 2. A slight difference is observed between results of Fig. 6(b) (with

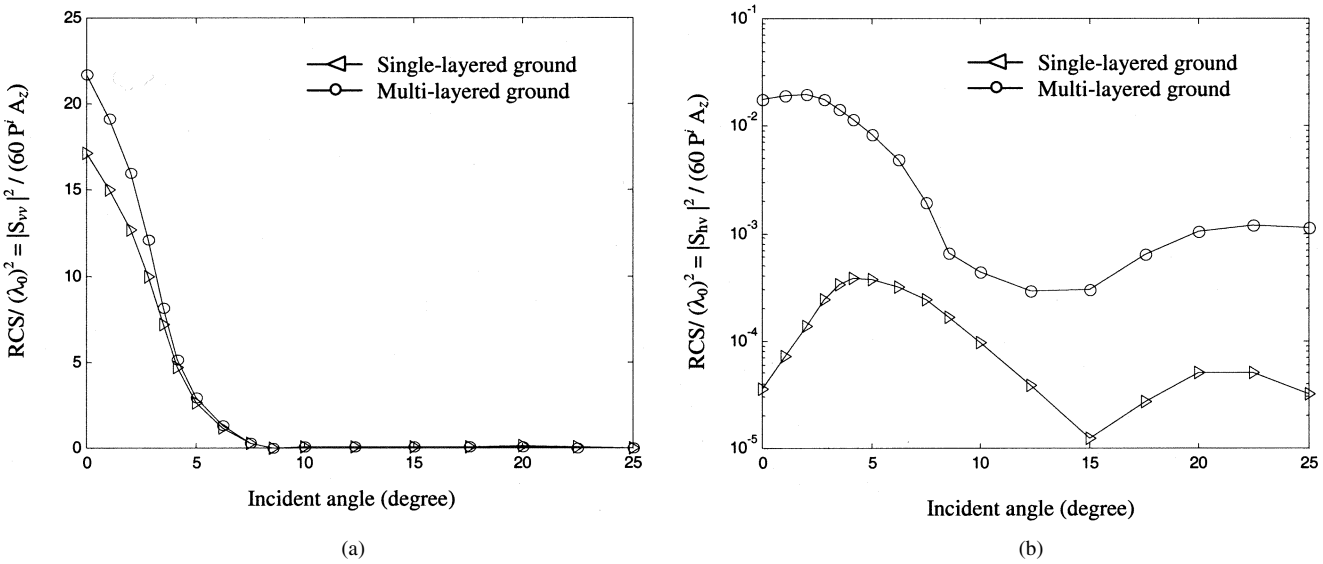

Fig. 8. Normalized RCS versus the incident angle θ^i for (a) VV and (b) HV, where the object is buried at $z = -0.3\lambda_0$, and $\varepsilon_{r2} = 2.5 - j0.18$, $\varepsilon_{r3} = 2.9 - j0.0092$, $\varepsilon_{r4} = 6.5 - j0.1$. The height is $H = 0.6\lambda_0$.

buried spheroid) and Fig. 6(c) (with no buried spheroid) due to the small size of the object as discussed in [11]–[15]. The results of Fig. 6(a)–(d) are almost independent of the polarization of the incident waves, since they are obtained at normal incidence, and of the buried object, due to its small size with respect to the wavelength.

The normalized RCS results in Fig. 7(a) are for a lossless rough/rough two-layered ground, with a buried spheroid ($a = c = 0.3\lambda_0$, $b = 0.15\lambda_0$ and $\varepsilon_{r3} = 2.9$), are plotted versus the height H for the H-polarization at normal incidence. All results in Fig. 7(a)–(c) are for the HH-polarization in the backscatter direction. In Fig. 7(b), the ground is assumed lossless rough/rough two-layer with $\varepsilon_{r2} = 6.5$. The RCS is plotted versus the dielectric constant of the underground layer, ε_{r4}, and height $H = 0.6\lambda_0$. The results show that the normalized HH-RCS increases with the increase of ε_{r4}. Fig. 7(c) shows results for lossless case versus the dielectric constant ε_{r2}, where an initial decrease is observed followed by monotonic increase with increasing ε_{r2}. The results show that the RCS has minimum value when $\varepsilon_{r2} \approx 4.2$, which could be due to destructive multiple interaction mechanism between the air- and underground interfaces.

In Fig. 8, the rough/rough ground is assumed lossy with $\varepsilon_{r2} = 2.5 - j0.18$, $\varepsilon_{r3} = 2.9 - j0.0029$, $\varepsilon_{r4} = 6.5 - j0.1$. The incident waves are assumed vertically polarized. The RCS is plotted versus incident angle θ^i where all results are in the backscatter direction ($\theta^i = \theta^s$, $\phi^i - \phi^s = \pi$). In Fig. 8(a) and (b), the normalized RCS for the VV- and the HV-polarization are plotted versus θ^i, respectively. These results are compared with those of a single-layer rough ground with the same buried spheroid, i.e., $\varepsilon_{r2} = \varepsilon_{r4} = 2.5 - j0.18$ and $\varepsilon_{r3} = 2.9 - j0.0029$. The results in Fig. 8(a) show the impact of the underground interface on the backscatter VV-RCS especially near normal incidence [16]. As expected, due to the small ground roughness considered in this work, the HV-RCS results are much smaller than those of the VV-polarization as shown in Fig. 8(b). The results in this case show that waves scattered from the two-layered rough ground exhibit more depolarization than those scattered from a single-layer ground. Similar results are obtained for the HH- and the VH-cases (not presented here).

It is important to emphasize that surface waves could be excited at the upper ground edges either due to the incident beam and/or due to the presence of the buried object which radiates spherical waves. However, these surface waves are insignificant due to the careful tapering of the incident waves in addition to the small size of the object compared with the ground surface.

IV. Conclusion

This paper investigated the polarimteric electromagnetic wave scattered from 2-D two-layered randomly rough ground with and without buried objects. The Monte Carlo simulations are conducted using the SDFMM to obtain the statistical average for the 3-D scattering problem. The statistical average of the fully polarimetric scattering matrix for the two-layer ground case is compared with that of the single-layer ground. The results show the significant effect on the scattered waves due to the multilayer nature of the rough ground demonstrated by the wave depolarization. Moreover, presenting the statistical average of the imaginary parts of the Covariance matrix elements enhances sensing the buried object despite of its small size compared with the free-space wavelength. It is difficult to draw one conclusion about scattering from the two-layer ground due to the large number of parameters affecting this mechanism such as the thickness of the upper layer, the relative dielectric constant of each layer and of the buried object, the roughness parameters of each interface, the incident and scattered directions and polarization, the object's burial depth and orientation, etc.

Current research is being conducted to develop processing techniques based on wave depolarization for detecting objects buried under individual rough surfaces, which should be of great interest to researchers working on this topic.

APPENDIX

The surface integral equations derived in [13] and [14] are

$$\overline{E}^{\,\mathrm{inc}}(\overline{r})\big|_{\mathrm{tang.}} = \left[(L_1+L_2)\,\overline{J}_1-(K_1+K_2)\,\overline{M}_1-L_3\overline{J}_2 +K_3\overline{M}_2-L_4\overline{J}_3+K_4\overline{M}_3\right]_{\mathrm{tang.}}, \quad \overline{r}\in S_1 \tag{A1}$$

$$\overline{H}^{\,\mathrm{inc}}(\overline{r})\big|_{\mathrm{tang.}} = \left[(K_1+K_2)\overline{J}_1+\left(\frac{L_1}{\eta_1^2}+\frac{L_2}{\eta_2^2}\right)\overline{M}_1-K_3\overline{J}_2 -\frac{L_3}{\eta_2^2}\overline{M}_2-K_4\overline{J}_3-\frac{L_4}{\eta_2^2}\overline{M}_3\right]_{\mathrm{tang.}}, \quad \overline{r}\in S_1 \tag{A2}$$

$$0 = \left[-L_2\overline{J}_1+K_2\overline{M}_1+(L_3+L_5)\,\overline{J}_2 -(K_3+K_5)\,\overline{M}_2+L_4\overline{J}_3-K_4\overline{M}_3\right]_{\mathrm{tang.}}, \quad \overline{r}\in S_2 \tag{A3}$$

$$0 = \left[-K_2\overline{J}_1-\frac{L_2}{\eta_2^2}\overline{M}_1+(K_3+K_5)\overline{J}_2 +\left(\frac{L_3}{\eta_2^2}+\frac{L_5}{\eta_3^2}\right)\overline{M}_2+K_4\overline{J}_3+\frac{L_4}{\eta_2^2}\overline{M}_3\right]_{\mathrm{tang.}}, \quad \overline{r}\in S_2 \tag{A4}$$

$$0 = \left[-L_2\overline{J}_1+K_2\overline{M}_1+L_3\overline{J}_2-K_3\overline{M}_2 +(L_4+L_6)\,\overline{J}_3-(K_4+K_6)\,\overline{M}_3\right]_{\mathrm{tang.}}, \quad \overline{r}\in S_3 \tag{A5}$$

$$0 = \left[-K_2\overline{J}_1+\frac{L_2}{\eta_2^2}\,\overline{M}_1+K_3\overline{J}_2+\frac{L_3}{\eta_2^2}\,\overline{M}_2 +(K_4+K_6)\overline{J}_3+\left(\frac{L_4}{\eta_2^2}+\frac{L_6}{\eta_4^2}\right)\overline{M}_3\right]_{\mathrm{tang.}}, \quad \overline{r}\in S_3 \tag{A6}$$

in which $\eta_i = \sqrt{\mu_i/\varepsilon_i}$ is the intrinsic impedance with $i = 1, 2, \ldots, 4$ and the integrodifferential operators L_j and K_j with $j = 1, 2, \ldots, 6$ are given in [13] and [14]. Similar to the MoM standard procedure, all the unknown electric and magnetic surface currents $\overline{J}$ and $\overline{M}$ in (A1)–(A6) are approximated using the vector basis function $\overline{j}\,(\overline{r})$ [21], [22] as

$$\overline{J}_k(\overline{r}) = \sum_{n=1}^{N_k} I_n^{(k)}\overline{j}_n^{\,(k)}(\overline{r})$$

$$\overline{M}_k(\overline{r}) = \eta_1\sum_{n=1}^{N_k} I_{(n+N_k)}^{(k)}\overline{j}_n^{\,(k)}(\overline{r}), \qquad \overline{r}\in S_k \tag{A7}$$

in which $k = 1, 2$ and 3 for surfaces S_1, S_2, and S_3, respectively. Substituting (A7) in (A1)–(A6), the linear system of equations $\overline{\overline{Z}}\,\overline{I} = \overline{V}$ is obtained.

REFERENCES

[1] L. Tsang, C. H. Chan, K. Pak, H. Sangani, A. Ishimaru, and P. Phu, "Monte Carlo simulations of large-scale composite random rough-surface scattering based on the banded-matrix iterative approach," *J. Opt. Soc. Amer. A*, vol. 11, no. 2, pp. 691–696, Feb. 1994.

[2] J. T. Johnson, L. Tsang, R. T. Shin, K. Pak, C. H. Chan, A. Ishimaru, and Y. Kuga, "Backscattering enhancement of electromagnetic waves from two-dimensional perfectly conducting random rough surfaces: A comparison of Monte Carlo simulations with experimental data," *IEEE Trans. Antennas Propagat.*, vol. 44, pp. 748–756, May 1996.

[3] E. Bahar and M. El-Shenawee, "Double scatter cross sections for two dimensional random rough surfaces that exhibit backscatter enhancement," *J. Opt. Soc. Amer. A*, vol. 18, no. 1, pp. 108–116, Jan. 2001.

[4] M. El-Shenawee and C. Rappaport, "Modeling clutter from Bosnian and Puerto Rican rough ground surfaces for GPR subsurface sensing applications using the SDFMM Technique," *J. Subsurface Sens. Technol. Appl.*, vol. 2, no. 3, pp. 249–264, July 2001.

[5] R. L. Wagner, J. Song, and W. C. Chew, "Monte Carlo simulation of electromagnetic scattering from two-dimensional random rough surfaces," *IEEE Trans. Antennas Propagat.*, vol. 45, no. 2, pp. 235–245, Feb. 1997.

[6] A. K. Fung, M. R. Shah, and T. Tjuatjia, "Numerical solution of scattering from three-dimensional randomly rough surfaces," *IEEE Trans. Geosci. Remote Sensing*, vol. 32, pp. 986–994, Sept. 1994.

[7] E. I. Thorsos, " The validity of the Kirchhoff approximation for rough surface scattering using a Gaussian roughness spectrum," *J. Acoust. Soc. Amer.*, vol. 83, pp. 78–92, 1988.

[8] S. O. Rice, "Reflection of electromagnetic waves from slighly rough surfaces," *Commun. Pure Appl. Math*, vol. 4, pp. 361–378, 1951.

[9] G. Zhang, L. Tsang, and K. Pak, "Angular correlation function and scattering coefficient of electromagnetic waves scattered by a buried object under a two-dimensional rough surface," *J. Opt. Soc. Amer. A*, vol. 15, no. 12, pp. 2995–3002, Dec. 1998.

[10] J. T. Johnson and R. J. Burkholder, "Coupled canonical grid/discrete dipole approach for computing scattering from objects above or below a rough interface," *IEEE Trans. Geosci. Remote Sensing*, vol. 39, pp. 1214–1220, June 2001.

[11] M. El-Shenawee, C. Rappaport, E. Miller, and M. Silevitch, "Three-dimensional subsurface analysis of electromagnetic scattering from penetrable/PEC objects buried under rough surfaces: Use of the steepest descent fast multipole method (SDFMM)," *IEEE Trans. Geosci. Remote Sensing*, vol. 39, pp. 1174–1182, June 2001.

[12] M. El-Shenawee, C. Rappaport, and M. Silevitch, "Monte Carlo simulations of electromagnetic wave scattering from random rough surface with 3-D penetrable buried object: Mine detection application using the SDFMM," *J. Opt. Soc. Amer. A*, vol. 18, no. 12, pp. 3077–3084, December 2001.

[13] M. El-Shenawee, "Scattering from multiple objects buried under two-dimensional randomly rough surface using the steepest descent fast multipole method," *IEEE Trans. Antennas Propagat.*, vol. 51, pp. 802–809, Apr. 2003.

[14] M. El-Shenawee and C. Rappaport, "Monte Carlo simulations for the statistics of clutter in minefields: AP mine-like target buried near a dielectric object beneath two-dimensional randomly rough ground," *IEEE Trans. Geosci. Remote Sensing*, vol. 40, pp. 1416–1426, June 2002.

[15] M. El-Shenawee, "Remote sensing of objects buried beneath 2-D random rough surfaces using the modified Mueller matrix elements," *J. Opt. Soc. Amer. A*, vol. 20, no. 1, pp. 183–194, January 2003.

[16] Y. Zhang and E. Bahar, "Mueller matrix elements that characterize scattering from coated random rough surfaces," *IEEE Trans. Antennas Propagat.*, vol. 47, pp. 949–955, May 1999.

[17] I. M. Fuks and A. G. Voronovoch, "Wave diffraction by rough surfaces in an arbitrary plane layered medium," *Waves Random Media*, vol. 10, pp. 253–272, 2000.

[18] J. Q. He, T. J. Yu, N. Geng, and L. Carin, "Method of moments analysis of electromagnetic scattering from a general three-dimensional dielectric target embedded in a multilayered medium," *Radio Sci.*, vol. 35, no. 2, pp. 305–313, Mar.–Apr. 2000.

[19] V. Jandhyala, "Fast multilevel algorithms for the efficient electromagnetic analysis of quasiplanar structures," Ph.D. dissertation, Dept. Elect. Comput. Eng., Univ. Illinois at Urbana-Champaign, 1998.

[20] P. Tran and A. A. Maradudin, "Scattering of a scalar beam from a two-dimensional randomly rough hard wall: Enhanced backscatter," *Phys. Rev. B*, vol. 45, no. 7, pp. 3936–3939, Feb. 1992.

[21] S. M. Rao, D. R. Wilton, and A. W. Glisson, "Electromagnetic scattering by surfaces of arbitrary shape," *IEEE Trans. Antennas Propagat.*, vol. 30, pp. 409–418, May 1982.

[22] L. Medgyesi-Mitschang, J. Putnam, and M. Gedera, "Generalized method of moments for three-dimensional penetrable scatterers," *J. Opt. Soc. Amer. A*, vol. 11, no. 4, pp. 1383–1398, April 1994.

[23] N. Garcia and E. Stoll, "Monte Carlo calculation for electromagnetic-wave scattering from random rough surfaces," *Phys. Rev. Lett.*, vol. 52, no. 20, pp. 1798–1801, May 1984.

[24] R. W. Freund, "A transpose-free quasiminimal residual algorithm for nonhermitian linear systems," *SIAM J. Sci. Comput.*, vol. 14, no. 2, pp. 470–482, Mar. 1993.

[25] J. Curtis, "Dielectric properties of soils; Various sites in Bosnia," U.S. Army Corp. Eng., Washington, DC, Waterways Experim., Station Data Rep., 1996.
[26] F. T. Ulaby, R. K. Moore, and A. K. Fung, *Microwave Remote Sensing Active and Passive*. Reading, MA: Addison-Wesley, 1981, vol. 1, Microwave Remote Sensing Fundamentals and Radiometry.
[27] C. A. Balanis, *Advanced Engineering Electromagnetics*: Wiley, 1989, ch. 6, pp. 254–309.
[28] W. C. Chew and C. C. Lu, "A fast algorithm to compute the wave-scattering solution of a large strip," *J. Comput. Phys.*, vol. 107, no. 2, pp. 378–387, Aug. 1993.
[29] F. T. Ulaby and C. Elachi, *Radar Polarimetry for Geoscience Applications*. Norwell, MA: Artech House, 1990.
[30] Y. Xu, R. M. Narayanan, X. Xu, and J. O. Curtis, "Polarimetric prosessing of coherent random noise radar data for buried object detection," *IEEE Trans. Geosci. Remote Sensing*, vol. 39, pp. 467–478, Mar. 2001.

Magda El-Shenawee (M'91–SM'02) received the B.S. and M.S. degrees from Assiut University, Assiut, Egypt, and the Ph.D. degree from the University of Nebraska–Lincoln, in 1991, all in electrical engineering.

In 1992, she was a Research Associate in the Center for Electro-Optics, University of Nebraska, where she focused on the problem of enhanced backscatter phenomena. In 1994, she was a Research Associate with the National Research Center, Cairo, Egypt, and in 1997, she was a Visiting Scholar with the University of Illinois at Urbana-Champaign. In 1999, she joined the Multidisciplinary University Research Initiative (MURI) at Northeastern University, Boston, MA. She is currently an Assistant Professor in the Department of Electrical Engineering, University of Arkansas, Fayetteville. Her research areas are rough surface scattering, computational electromagnetics, subsurface sensing of buried objects, breast cancer modeling, numerical methods, and microstrip circuits.

Dr. El-Shenawee is a member of the Eta Kappa Nu electrical engineering honor society.